J|A|C|S
ARTICLES

Published on Web 05/28/2009

Structural Characterization of Pt−Pd and Pd−Pt Core−Shell Nanoclusters at Atomic Resolution

Sergio I. Sanchez,[†] Matthew W. Small,[†] Jian-min Zuo,[‡] and Ralph G. Nuzzo*[,†]

Department of Chemistry and the Frederick Seitz Materials Research Laboratory, University of Illinois at Urbana−Champaign, Urbana, Illinois 61801, and Department of Materials Science and Engineering, University of Illinois at Urbana−Champaign, Urbana, Illinois 61801

Received March 17, 2009; E-mail: r-nuzzo@illinois.edu

Abstract: We describe the results of a study at atomic resolution of the structures exhibited by polymer-capped monometallic and bimetallic Pt and Pd nanoclusters—models for nanoscale material electrocatalysts—as carried out using an aberration-corrected scanning transmission electron microscope (STEM). The coupling of sub-nanometer resolution with *Z*-contrast measurements provides unprecedented insights into the atomic structures and relative elemental speciation of Pt and Pd within these clusters. The work further defines the nature of deeply quenched states that prevent facile conversions of core−shell motifs to equilibrium alloys and the nature of nonidealities such as twinning (icosahedral cores) and atomic segregation that these structures can embed. The nature of the facet structure present in these model systems is revealed by theory directed modeling in which experimental intensity profiles obtained in *Z*-contrast measurements at atomic resolution are compared to simulated intensity profiles using theoretically predicted cluster geometries. These comparisons show close correspondences between experiment and model and highlight striking structural complexities in these systems that are compositionally sensitive and subject to amplification by subsequent cluster growth processes. The work demonstrates an empowering competency in nanomaterials research for STEM measurements carried out using aberration corrected microscopes, approaches that hold considerable promise for characterizing the structure of these and other important catalytic materials systems at the atomic scale.

Introduction

Understandings of homogeneous and heterogeneous catalysis have benefited greatly from the insights into materials structure developed through the use of electron microscopy.[1−4] Using this analytical technique, it is possible to determine features critical to catalytic performance that include supported catalyst particle mass distributions,[5−8] crystallographic structure,[1,3,4,9,10] and the speciation of specific forms of structural complexity and/or defects.[11−14] Beyond such visual and diffraction centric forms of analysis, there have evolved additional techniques that strongly compliment and extend the analytical capacities of electron microscopy—ones yielding information pertaining to the chemical nature of catalytic materials, as well as their electronic structure.[15−19] Energy dispersive X-ray spectroscopy (EDS) and electron energy loss spectroscopy (EELS) are among the more common techniques paired with imaging and diffraction that serve to offer such forms of compositional and chemical information.[14,15]

The deep capacities for structural characterization that analytical electron microscopy provides for studies of catalysts notwithstanding, there still remain some important limitations. The use of EDS to quantitatively probe the composition of materials, for example, is limited by the low detector collection efficiency. For small nanoparticles, the electron dosage required

[†] Department of Chemistry and the Frederick Seitz Materials Research Laboratory.
[‡] Department of Materials Science and Engineering.

(1) Chen, J.; Lim, B.; Lee, E.; Xia, Y. *Nano Today* **2009**, *4*, 81–95.
(2) Li, Z.; Yound, N.; Di Vece, M.; Palomba, S.; Palmer, R.; Bleloch, A.; Curley, B.; Johnston, R.; Jiang, J.; Yuan, J. *Nature* **2008**, *451*, 46.
(3) Bratlie, K. M.; Lee, H.; Komvopoulos, K.; Yang, P.; Somorjai, G. A. *Nano Lett.* **2007**, *7*, 3097–3101.
(4) Lee, H.; Habas, S. E.; Kweskin, S.; Butcher, D.; Somorjai, G. A.; Yang, P. *Angew. Chem., Int. Ed.* **2006**, *45*, 7824–7828.
(5) Claus, P.; Bruckner, A.; Mohr, C.; Hofmeister, H. *J. Am. Chem. Soc.* **2000**, *122*, 11430–11439.
(6) Li, Y.; Boone, E.; El-Sayed, M. *Langmuir* **2002**, *18*, 4921–4925.
(7) Weber, A.; Seipenbusch, M.; Kasper, G. *J. Nanopart. Res.* **2003**, *5*, 293–298.
(8) Teranishi, T.; Hosoe, M.; Miyake, M. *Adv. Mater.* **1997**, *9* (1), 65–67.
(9) Baiker, A.; Grunwaldt, J.; Muller, C.; Schmid, L. *Chimia* **1998**, *52*, 517–524.
(10) Mahmoud, M.; Tabor, C.; El-Sayed, M.; Ding, Y.; Wang, Z. *J. Am. Chem. Soc.* **2008**, *130*, 4590–4591.
(11) Schauermann, S.; Hoffmann, J.; Johanek, V.; Hartmann, J.; Libuda, J.; Freund, H. *Catal. Lett.* **2002**, *84*, 209–217.
(12) Lorenz, C.; Haghgooie, R.; Kennebrew, C.; Ziff, R. *Surf. Sci.* **2002**, *517*, 75–86.
(13) Gates, B.; Knozinger, H. *Impact of Surface Science on Catalysis*; Academic Press: San Diego, 2000; pp 49−51.
(14) Williams, D. B.; Carter, B. C. *Transmission Electron Microscopy: Basics*; Springer Science+Business Media Inc.: New York, 1996.
(15) Goodhew, P.; Humphreys, J.; Beanland, R. *Electron Microscopy and Analysis*, 3rd ed.; Taylor and Francis: London, 2001; pp 76−80.
(16) Li, H.; Sun, G.; Li, N.; Sun, S.; Su, D.; Xin, Q. *J. Phys. Chem. C* **2007**, *111*, 5605–5617.
(17) Hills, C. W.; Mack, N. H.; Nuzzo, R. G. *J. Phys. Chem. B* **2003**, *107*, 2626–2636.
(18) Hills, C. W.; Nashner, M. S.; Frenkel, A. I.; Shapley, J. R.; Nuzzo, R. G. *Langmuir* **1999**, *15*, 690–700.
(19) Nashner, M. S.; Frenkel, A. I.; Adler, D. L.; Shapley, J. R.; Nuzzo, R. G. *J. Am. Chem. Soc.* **1997**, *119*, 7760–7771.

for successful EDS analysis is often too high and beyond the radiation damage thresholds of nanoparticles.[20] The dearth of knowledge concerning the surface structures (and composition) of small particles—features that are difficult to characterize by microscopy—also presents a major hindrance to progress in correlating such aspects with catalytic response to provide an atomistically rationalized basis for the formulation of predictive structure−property and structure−rate correlations in heterogeneous catalysis. This shortcoming is particularly significant given the likely emergence of important forms of mesoscopic behaviors in material systems in this size range. In addition to such pictures related to the size of a catalyst particle, which can elicit changes to a cluster's bonding geometry and catalytic behavior,[3,21,22] hybrid structures such as bi(multi-)metallic catalysts present additional forms of complexity where the nature and bonding of a metal surface is altered by the specific placements adopted by the different atoms of a binary (or higher) composition.[23,24] Such changes from homo- to heterometallic coordination,[25−28] in combination with the strain associated with lattice mismatches,[23,24] can further contribute to modifications of the catalytic nature of a material and, unfortunately for all but highly specialized model systems, remain very poorly understood. This larger deficiency provides a strong motivation for work seeking to provide a more thorough understanding of a catalyst's structure at the atomic scale, the focus of the work reported here.

The conventional use of high-angle-annular-dark-field scanning transmission electron microscopy (HAADF-STEM) allows one to probe the microstructures of catalytic materials with resolution of a few Ångstroms.[15] This method relies on the detection of electrons that are scattered at high angles relative to the transmitted beam (Rutherford scattering) using an annular detector.[14,29] At large scattering angles the scattering intensity is strongly and quantitatively dependent on the atomic number (Z) of the element interacting with the electron beam, varying proportionally to Z^x and with the thickness of the material (i.e., number of stacked atoms).[29,30] The power factor, X, equals 2 for Rutherford scattering in the limit of electron single scattering. Electron multiple scattering and electron probe propagation in thick samples can lead to values of X that are lower than 2. Nonetheless, the image contrast remains strongly dependent on Z.[31] This strong dependence on Z provides the quantitative foundation for so-called Z-contrast imaging; a technique that allows high-contrast imaging of high-Z elements (such as the noble metals in a heterogeneous catalyst) against the background of a low-Z material (such as a support phase).[32] Such Z-contrast imaging results in more accurate size and composition determinations as compared to conventional bright-field transmission electron microscopy.[14]

The present work explores the exceptional analytical capacities of Z-contrast microscopy extended to the limit of atomic resolution, applying it to the study of model binary clusters of interest in electrocatalysis.[16,33] The data presented in this report follow from the advent of the spherical aberration (C_s) corrected electron microscopes, that provide dramatic improvements in image quality (sub-Ångstrom resolution and improved signal-to-noise ratios from the use of a large condenser aperture), pushing the limitations of atomic scale imaging and fostering new capacities for atomic level speciation of complex bonding motifs for materials.[34−38] The enhancements afforded by C_s-corrected imaging are making accessible unprecedented forms of information regarding atomic scale structural features as well as enabling the discernment of elemental composition within a sample when employed in the HAADF-STEM mode.[2,29,30,39]

This work utilizes these latter competencies, providing structural characterizations of Pd−Pt and Pt−Pd core−shell nanoclusters at atomic resolution. Recent work has exploited similar capacities to specify elemental variations within alloyed Pt−Co nanoparticles.[39] In that study, line scans mapping the intensity across the diameter of the particles showed random fluctuations in the intensity of neighboring peaks, fluctuations ascribable to scattering from lower (Co) and higher (Pt) Z elements within a cluster. In work conducted by Li et al.,[2] an intensity diagram (obtained using a sub-Ångstrom probe) was combined with HAADF-STEM simulations to gain insight into the geometry of Au nanoparticles deposited by a soft-landing method onto an amorphous carbon support. Comprehensive studies conducted by Rosenthal et al. made use of the Z-contrast imaging and modeling to characterize compositional and structural features of biologically active Cd−Se nanoparticles.[29] This latter study utilized Rutherford backscattering experiments and intensive imaging techniques to index the crystal facet planes of the Cd−Se/Zn−S nanocrystals and identify hierarchical structural motifs related to their core−shell structure.

In this report we use controlled synthetic techniques and C_s-corrected imaging to describe the atomic structure and elemental segregation of both monometallic and bimetallic Pt and Pd nanoparticles, materials currently utilized as electrocatalysts.[16,33] Using modifications of literature methods,[40] we synthesized and subsequently analyzed Pt(core)−Pd(shell) and Pd(core)−Pt(shell) nanoparticles with cluster diameters lying in the range of 2−4 nm. Empirical examinations of the images and more quantitative analyses of integrated intensity profiles, when

(20) Huang, W. J.; Zuo, J. M.; Jiang, B.; Kwon, K. W.; Shim, M. *Nature Phys.* **2008**, *5*, 129–133.
(21) Haruta, M. *Chem. Rec.* **2003**, *3*, 45–87.
(22) Mayrhofer, K. J. J.; Blizanac, B. B.; Arenz, M.; Stamenkovic, V. R.; Ross, P. N.; Markovic, N. M. *J. Phys. Chem. B* **2005**, *109*, 14433–14440.
(23) Rodriguez, J. A.; Goodman, D. W. *Science* **1992**, *257*, 897–903.
(24) Sinfelt, J. H. *Bimetallic Catalysts: Discoveries, Concepts, and Applications*; John Wiley and Sons, Inc.: New York, 1983.
(25) Mavrikakis, M.; Hammer, B.; Norskov, J. K. *Phys. Rev. Lett.* **1998**, *81* (13), 2819–2822.
(26) Jakob, P.; Gsell, M.; Menzel, D. *J. Chem. Phys.* **2001**, *114* (22), 10075–10085.
(27) Gsell, M.; Jakob, P.; Menzel, D. *Science* **1998**, *280*, 717–720.
(28) Menard, L.; Xu, F.; Nuzzo, R.; Yang, J. *J. Catal.* **2006**, *243*, 64.
(29) Rosenthal, S.; McBride, J.; Pennycook, S.; Feldman, L. *Surf. Sci. Rep.* **2007**, *62*, 111.
(30) Browning, N. D.; Chisholm, M. F.; Pennycook, S. J. *Nature* **1993**, *366*, 143–146.
(31) Xu, X.; Saghi, Z.; Gay, R.; Mobus, G. *Nanotechnology* **2007**, *18*, 1–8.
(32) Singhal, A.; Yang, J. C.; Gibson, J. M. *Ultramicroscopy* **1997**, *67*, 191–206.
(33) Yang, J.; Lee, J. Y.; Zhang, Q.; Zhou, W.; Liu, Z. *J. Electrochem. Soc.* **2008**, *155*, B776–B781.
(34) Haider, M.; Uhlemann, S.; Schwan, E.; Rose, H.; Kabius, B.; Urban, K. *Nature* **1998**, *392*, 768–769.
(35) Nellist, P. D.; Chisholm, M. F.; Dellby, N.; Krivanek, O. L.; Murfitt, M. F.; Szilagyi, Z. S.; Lupini, A. R.; Borisevich, A.; Sides, W. H., Jr.; Pennycook, S. J. *Science* **2004**, *305*, 1741.
(36) Batson, P. E.; Dellby, N.; Krivanek, O. L. *Nature* **2002**, *418*, 617–620.
(37) Freitag, B.; Kujawa, S.; Mul, P. M.; Ringnalda, J.; Tiemeijer, P. C. *Ultramicroscopy* **2005**, *102*, 209–214.
(38) Borisevich, A.; Lupini, A. R.; Travaglini, S.; Pennycook, S. J. *J. Electron Microsc.* **2006**, *55*, 7–12.
(39) Chen, S.; Ferreira, P.; Sheng, W.; Yabuuchi, N.; Allard, N.; Shao-Horn, Y. *J. Am. Chem. Soc.* **2008**, *130*, 13818–13819.
(40) Wang, Y.; Toshima, N. *J. Phys. Chem. B* **1997**, *101*, 5301–5306.

developed in conjunction with theory supported modeling, provides deep insights into the atomic-level structural features present in these model binary metal nanostructures. We find striking, and also surprising, morphological differences between the monometallic Pt and Pd nanoparticles—a divergence in structure that is also reflected in and amplified by the structures of the bimetallic clusters formed from them via a seeded nucleated growth process. Power spectra, Fourier transforms (FT) of the atomic resolution images, allow derivation of crystallographic data that in turn allow the assignment of truncating planes, crystal orientations, and specific forms of nanoparticle structure that are sensitive to and reflect the nature of metastable states in materials at this scale. The present data collectively support the importance of dynamical models—energy landscapes—to the atomic structures of metal nanoparticle catalysts and, potentially, for their catalytic behaviors as well.

Experimental Section

Nanoparticle Preparation. Polyvinylpyrrolidone (MW = 40 000 g/mol) (PVP)-capped monometallic Pt and Pd nanoparticles were synthesized using an alcohol reduction method. Metal precursors [266 mg of H_2PtCl_6 (FW = 409.82 g/mol) or 136 mg of $Pd(OAc)_2$ (FW = 224.50 g/mol) for Pt and Pd, respectively] were independently refluxed in a 300 mL ethylene glycol solution in the presence of 2.5 g of PVP. Removal of excess PVP was accomplished by centrifuging aliquots of the PVP-capped Pt (or Pd) nanoparticle solution with 5 equiv of acetone. After centrifugation, the isolated particles were resuspended and stored in ethanol.

The synthesis of core−shell nanoparticles was carried out using a method similar to that previously described by Toshima et al.,[40] one involving the use of a "sacrificial hydrogen layer." The premade, ethanol-stored monometallic Pt (or Pd) nanoparticles were flushed with ultrahigh purity H_2(g) for 3 h followed by the purging of unadsorbed H_2 with N_2(g) (2 h). Solutions of the hydrogen-coated Pt nanoparticles were then treated with a dilute degassed solution containing appropriate amounts $Pd(OAc)_2$ (∼0.38 mM) dissolved in an acetone/H_2O mixture. Premade Pd nanoparticles were treated with a dilute degassed solution (∼0.34 mM) containing appropriate amounts of H_2PtCl_6(aq). The addition of the secondary metal solution in each case was paced at a rate no faster than 20 mL/h under a N_2 flow.

A random alloy was obtained by the coreduction of 271 mg of H_2PtCl_6 and 117 mg of $PdCl_2$ (FW = 177.31 g/mol) refluxed in a 300 mL methanol/H_2O mixture (1:1, v/v) degassed (N_2) solution containing PVP (3.02 g). All chemicals were purchased from Sigma-Aldrich.

Electron Microscopy. Samples for low-magnification STEM imaging were prepared by dip-coating a holey carbon film supported on a Cu grid (SPI Supplies) into the nanoparticle suspensions. Size and EDS measurements were made on individual nanoparticles to ensure the presence of Pt and Pd atoms using a JEOL model 2010F electron microscope operated at 200 keV equipped with an Oxford INCA 30 mm ATW detector for energy dispersion X-ray spectroscopy. The instrument used an electron beam focused to 0.5 nm as a probe during individual nanoparticle sizes and EDS measurements of the Pd L_3 and Pt M edges. The average sizes for the monometallic Pt and Pd nanoparticles were 2.36 ± 0.44 and 2.44 ± 0.37 nm, respectively (Supporting Information, Figure 1). The average sizes for the bimetallic nanoparticle samples were; 3.29 ± 0.62, 3.53 ± 0.64, and 2.49 ± 0.47 nm corresponding to the Pt(core)−Pd(shell), Pd(core)−Pt(shell), and Pt−Pd alloy samples, respectively (Supporting Information, Figure 2). The Pt(core)−Pd(shell) nanoparticles prepared at a 1:1 ratio (Pt/Pd) gave values of 49 at. % Pt with 51 at. % Pd (1.0% error), respectively. The Pd(core)−Pt(shell) nanoparticles prepared at a 1:1 ratio (Pd/Pt) afforded corresponding EDS values of 53 at. % Pd with 47 at. % Pt (2.4% error). The alloy yielded bulk EDS results of 45 at. % Pt with 55 at. % Pd (3% error). Taken together these results present data in line with expectations based on the stoichiometric ratios used in the synthesis process. Particle sizes were determined by measuring the diameter cross-section of individual particles using DigitalMicrograph (Gatan Inc.) software. Samples for C_s-corrected imaging were similarly prepared by dip-coating ultrathin holey carbon films (Ted Pella Inc.) supported on Cu grids into the colloidal suspensions. These images were obtained using a JEOL model 2200-FS electron microscope operated at 200 keV.

Theoretical Modeling. Several software programs were used to analyze and simulate the HAADF-STEM data. The structures of idealized crystals were created and manipulated using the Visual Molecular Dynamics (VMD)[41] program to provide a structure that more accurately reflected the appearance of the experimental images. Optimized crystal structures were then deduced using the STEM image simulation program (ZMULT) developed by Zuo. This program is based on the multislice method of Cowley and Moodie.[42,43]

For the crystals under consideration, lattice constants of Pt (3.92 Å) and Pd (3.89 Å)[44] were used for cuboctahedral and icosahedral structures, respectively (see below). Models for both mono- and bimetallic nanoparticles were created on the basis of these two limiting structural forms. For the bimetallic structures, the core structure was used to dictate the overall conformation of the particle. For the case of the Pd(core)−Pt(shell), this required that the Pd core was taken to be an icosahedron, whereas the Pt(core)−Pd(shell) structure had the growth of the Pd atoms occurred on a cuboctahedral core structure (see below).

To provide meaningful comparisons with the experimental data, the simulated structures were rotated such that the orientation of the nanoparticle used for the simulation was identical to that determined via analysis of the experimental image FT. This alignment was checked by validating that the FT of the simulated crystal's projected potential gave the appropriate spatial frequencies. It should be noted that this procedure was not possible for the icosahedral particles due to the extensive twinning present in that case.

Scans were conducted using a box with an edge length 20 Å larger than the largest crystal examined. This box was then pixilated into a 512 × 512 region. Within this area, a sector of interest was chosen that comprised 10% of the *y*-axis (centered on the crystal) and 100% of the *x*-axis. Scanning/simulation of this region produced a potential map that was analyzed using DigitalMicrograph (Gatan, Inc.) for subsequent comparison with the experimental intensity profiles of the same region of the crystal.

X-ray Diffraction. Details regarding the collection of the synchrotron radiation X-ray diffraction can be found in the Supporting Information (Experimental Details for XRD Measurements).

Results and Discussion

Figure 1a shows a representative C_s-corrected HAADF-STEM image of a PVP-protected Pt nanoparticle. The inset to the figure is the FT (diffraction data) of the cluster, which indicates a [001] zone axis with the evident (002) lattice planes as indexed in the image. The sharp peaks in the FT indicate that a well ordered crystalline state characterizes these samples. A tabulation of the diffraction data for all samples analyzed is given in the Supporting Information (Tables 1 and 2). Several general trends

(41) Humphrey, W.; Dalke, A.; Schulten, K. *J. Molec. Graphics* **1996**, *14*, 33–38.
(42) Holmestad, R.; Jiang, B.; Zuo, J. M. In *STEM Contrast in Perovskite Materials*; 16th International Microscopy Congress, Sapporo, Japan: Sapporo, Japan, 2006; p 608.
(43) Zuo, J. M.; Huang, W. J.; Shah, A.; Kroeger, R. *Microsc. Microanal.* **2008**, *14*, 920–921.
(44) *CRC Handbook of Chemistry and Physics*, 75th ed.; CRC Press: Boca Raton, FL, 1995.

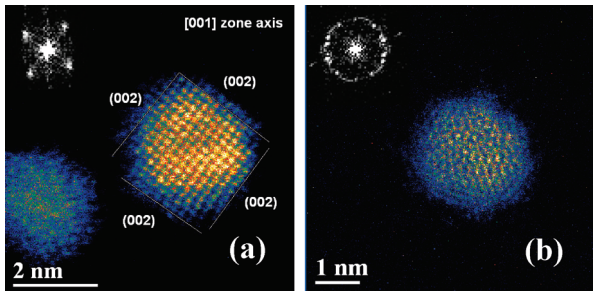

Figure 1. Representative C_s-corrected HAADF-STEM images of PVP-capped monometallic (a) Pt and (b) Pd nanoparticles. The inset power spectra were obtained from their respective images. The solid lines in (a) identify the facet planes revealed by the power spectrum data.

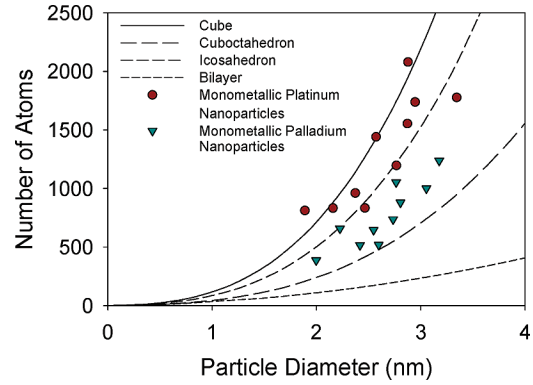

Figure 2. Atom count measurements for 10 monometallic Pt and Pd nanoparticles (symbols) plotted as a function of their experimentally measured diameter. The lines depict different, ideal geometries. For the case of the cube and cuboctahedron these represent the smallest geometric diameter. However, the icosahedron diameter was chosen to be the mean of the maximum and minimum theoretical diameters due to the difficulty of accurately distinguishing between these dimensions within the experimental images. Finally, the bilayer was viewed as the top of a truncated cube, dictating that the diameter be measure as the length of an edge when viewed from above.

are evidenced there. The Pt particles supported on the carbon film of the TEM grid were generally found to be oriented along either the [001] or the [011] zone axes, consistent with the polyhedral forms predicted by theory to be the most stable (cuboctahedron and cubes, respectively, Supporting Information, Figure 3).[1,45,46] Integrated areal intensity profile measurements and modeling describing the atomic structure of a particular Pt particle shown are given in Supporting Information Figure 4. The areal scans reflecting the number of Pt atoms lying within a single column, show a typical (and expected) hemispherical profile as the cluster diameter is traversed (quantitatively, the lower intensities at the peripheries indicate that fewer atoms are stacked at these positions). The model (Supporting Information, Figure 4b) quantitatively replicates these effects by using the specific crystal orientation and truncating planes shown in Supporting Information, Figure 4a. The profiles are those expected for a cuboctahedron cluster structure. The experimental and simulated profiles show clearly discernible peaks, thereby enabling the measurement of interatomic pair distances by calculating the separation between intensity peaks up to the limit of the microscope scan precision. This analysis suggests a lattice constant for the Pt particles of 3.8 $\pm$ 0.2 Å along the [001] zone axis (Figure 1a), a value within the uncertainty limit of literature values for bulk Pt (3.92 Å).[44]

The structures adopted by monometallic Pd nanoparticles are far more complex, their structures can be described using models of crystals embedded with a multitude of defects in the form of twins and dislocations (Figure 1b and Supporting Information, Figure 5). Figure 1b shows a representative image of such a Pd nanoparticle. The image FT (inset) shows that these samples lack the single-crystalline qualities exhibited by the Pt clusters. The pattern in the inset demonstrates a noncrystallographic spectrum and significant broadening of the spatial frequencies in the FT as a consequence of the much finer crystalline grain, and multiple domains, that in turn result in a more ambiguous demonstration for the truncating lattice planes at the surface (Supporting Information, Figure 5). Examinations of intensity profiles for the Pd clusters revealed Gaussian-like shapes, a finding qualitatively similar to that of the Pt cluster, albeit with the distinction that the spacings between atomic planes can not be resolved for the more distorted Pd particles. The disorder exhibited by the monometallic Pd nanoparticles can be explained by unusual examples of structural disorder imparted by the dimensional confinement of the particle as it decreases in size from its bulk state. One such example was offered by Gilbert et al.[47] where competitive forces of surface relaxation give rise to "inhomogeneous internal strain". Alternatively, it has been noted that Pd tends to adopt either an icosahedral or decahedral conformation within this size regime.[48,49] Using Zmult we obtained the projected potential for both icosahedral and decahedral structures at various orientations. Repeated application of a Gaussian blur convolution to the projected potentials allowed us to make semiquantitative comparisons between the areal intensity maps of experimental images and images with similar appearances generated from the projected potential (Supporting Information, Figure 6). Of the many images we were able to model using this protocol, we found that the structures of these monometallic Pd nanoparticles were best defined by an icosahedron. These simulations of experiment—representative examples of which are provided in Supporting Information Figure 6—specifically show projections of symmetries (including the 2-fold axis) expected for icosahedra.

The samples in Figure 1a and b can be further modeled quantitatively to provide an estimation of the number of atoms contained within the particles, we analyzed images of many representative particles using the DigitalMicrograph program (Gatan, Inc.). By taking an average of the background-corrected intensity of a number of single atoms visible within an image, it is possible to calculate an average single atom scattering intensity calibration for each image (Supporting Information, Figure 7). The averaged atom counts vs cluster diameter data for the monometallic Pt and Pd particles examined are presented in Figure 2. The results given in Figure 2 clearly suggest some form of structure whose atomic ordering lies between the limits defined by cubic and cuboctahedral structures, a conclusion anticipated by previous work.[1,45,46,48,49] We observe a structural divergence as mediated by the nature of the material. For the Pt nanoparticles, the crystal growth can be modeled by that of

(45) Petroski, J.; Wang, Z.; Green, T.; El-Sayed, M. *J. Phys. Chem. B* **1998**, *102*, 3316–3320.
(46) Song, H.; Kim, F.; Connor, S.; Somorjai, G.; Yang, P. *J. Phys. Chem. B* **2005**, *109* (1), 188–193.
(47) Gilbert, B.; Huang, F.; Zhang, H.; Waychunas, G. A.; Banfield, J. F. *Science* **2004**, *305*, 651–654.
(48) Jose-Yacaman, M.; Marin-Almazo, M.; Ascencio, J. *J. Mol. Catal. A: Chem.* **2001**, *173*, 61.
(49) Lim, B.; Xiong, Y.; Xia, Y. *Angew. Chem., Int. Ed.* **2007**, *46*, 9279–9282.

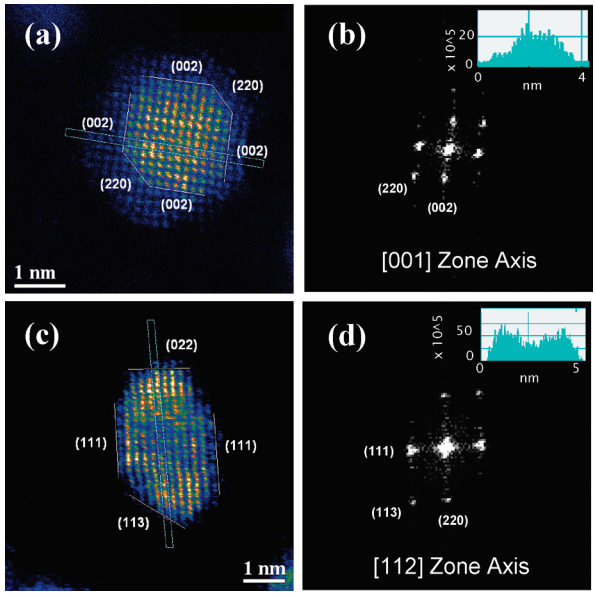

Figure 3. Bimetallic nanoparticles synthesized using a sacrificial hydrogen layer. (a) Image of a Pt(core)−Pd(shell) nanoparticle complete with labeled crystal facets and the areal integrated intensity measurement made within the boxed region. Power spectrum data and annotated zone axis with the intensity profile represented as the inset in (b). (c) Pd(core)−Pt(shell) nanoparticle with defined truncating planes and areal integrated intensity measurement made within the boxed region. Corresponding power spectrum data and integrated intensity profile measurement shown as the inset in (d).

a cubic structure. Conversely, growth of Pd nanoparticles is bounded by icosahedral and cuboctahedral size dependences.

It is useful to consider the structural dissimilarities evidenced in these data and ask whether they might hold any resultant importance for catalytic behavior. For the Pt clusters, we observe well organized, single-crystalline structures accompanied by well-defined, truncating facets. Such motifs provide support for allocating structure−function properties to the cluster for structurally sensitive catalytic pathways, such as was previously shown for different geometrically shaped Pt nanoparticles by Chen et al.[1] The situation for the Pd nanoparticles is far more complex, with the structures evidencing a significant degree of atomic disorder and bond strain. The lower degree of crystallinity for the Pd nanoparticles found here is supported by the results of past studies using X-ray-based measurements of the atomic pair distribution function (PDF).[50,51] The data suggest rate/property correlations that, in this case, would have to more fully consider the roles that might be played in reaction mechanisms by a richer population of structural defects.

The materials described above were then used to nucleate the growth of a secondary metal shell. In the one instance this was Pt on a Pd core and in the other Pd on a Pt core.[40] Figure 3 shows representative images of these bimetallic Pt(core)−Pd(shell) and Pd(core)−Pt(shell) nanoparticles as synthesized using a sacrificial hydrogen layer to mediate the growth.[40] The image in Figure 3a is exemplary of the structures adopted by Pt(core)−Pd(shell) nanoparticles, core−shell clusters that exhibit an exceptionally high contrast region in the HAADF-STEM image localized at its center. This demonstrates the retention

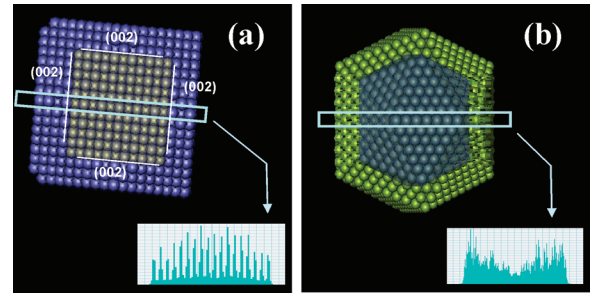

Figure 4. Simulated bimetallic nanoparticles modeling the (a) Pt(core)−Pd(shell) and the (b) Pd(core)−Pt(shell) samples. The Pt(core)−Pd(shell) sample was directly modeled using crystallographic data to mimic the image seen in Figure 3a with intensity scan (boxed region) and corresponding profile (inset in (a)). An icosahedral structure was assumed for the Pd(core)−Pt(shell) sample with attendant line scan (boxed region) and intensity profile (the inset in (b)).

of the Pt atoms within the cluster core. The spatial frequencies obtained from the image FT (Figure 3b) suggests that the particle is aligned along its [001] zone axis, which in turn allows the assignment of the various facet planes present (solid lines in Figure 3a). For these samples the most abundant zone axis found in these images was along the [011] direction with (111) and (002) facets being the most abundant truncating lattice planes (Supporting Information, Tables 1 and 2). Another important feature regarding these images is the Pd atoms use of the Pt core as a template for what appears to be an essentially epitaxial, and reasonably defect-free, form of overlayer growth. Evidence for this interpretation is provided by comparisons made between the data given in Figures 1a and 3a, where one notes the same truncating edges are exhibited for the shell and the core structures. Such trends epitomize the requirements for pseudomorphic growth[23,52] and we conclude, as such, that the Pd atoms of the shell coherently match the lattice structure of the Pt core. This interpretation is well supported by the broader data taken from many clusters in the sample (Supporting Information, Figure 8). The boxed region in Figure 3a presents an integrated intensity measurement made of the cluster (inset of Figure 3b). Surrounding the high intensity core region are areas significantly lower in intensity, ones presumably attributable to the lower Z Pd atoms. Such intensity profiles were consistently seen for the clusters in these Pt(core)−Pd(shell) samples (Supporting Information, Figure 8).

Computer simulations of the HAADF-STEM potential were carried out to support these interpretations more quantitatively using an ideal Pt cuboctahedron structure oriented along its [001] zone axis with (002) facets terminating the crystal edges as the basis for the calculations. To mimic the image seen in Figure 3a, multiple layers of Pd atoms were added around this Pt core (Figure 4a). The projected potential of the simulated crystal was found to provide a reasonable representation of the actual image. Beyond the aesthetic appeal of the model, however, the simulated areal intensities of the cluster (inset of Figure 4a) exhibit profiles closely resembling those of experiment (e.g., the inset of Figure 3b). We see, for example, that there is a sharp decrease in the intensity of the edge peaks in comparison to the central region. This follows both the qualitative and quantitative contours of experiment. These data affirm the structure of a pseudomorphic cluster of high-*Z* Pt atoms encased by those of a lower-*Z* Pd shell.

(50) Petkov, V.; Bedford, N.; Knecht, M.; Weir, M.; Crooks, R.; Tang, W.; Henkelman, G.; Frenkel, A. *J. Phys. Chem. C* **2008**, *112*, 8907.
(51) Petkov, V.; Ohta, T.; Hou, Y.; Ren, Y. *J. Phys. Chem. C* **2007**, *111*, 714–720.
(52) Van Hove, M. A.; Tong, S. Y. *The Structure of Surfaces*; Springer: New York, 1985.

A strong templating effect is also seen in the inverse plating sequence. Representative data for a Pd(core)−Pt(shell) nanoparticle and its corresponding FT are shown in panels c and d of Figure 3, respectively. The pattern in Figure 3d indicates a [112] zone axis with the associated facets as annotated in Figure 3c. It is worth noting the presence of high index lattice planes truncating the particle in this case. For example, the (113) and (022) lattice planes are clearly discernible on this representative particle. These truncations are generally associated with higher surface energies[1,53] for the facet structures, a surprising but not completely unprecedented outcome.[39] We also note the attendant differences between the image in Figure 3c and its Pt(core)−Pd(shell) analogue (Figure 3a), observed here as an inversion of the intensity map. The greater contribution to the integrated intensity that resides at the periphery of these clusters implies a strong biasing placement of the Pt atoms at the exterior of the particle. A concave-shaped profile was observed for essentially all Pd(core)−Pt(shell) nanoparticles in the sample (Supporting Information, Figure 9). We also found that the Pd nanoparticles do not generally sustain isotropic heteroepitaxy in the growth of the Pt overlayer. With the Pd(core)−Pt(shell) samples, we instead see more sporadic/discontinuous (perhaps nodular) plating of the Pt atoms onto the Pd core (Supporting Information, Figure 9). The images given in Supporting Information Figure 9 show different examples of Pt coverage unevenly distributed over the Pd core's surface. Areal scans of these clusters (inset in Figure 3d and Supporting Information Figure 9) show the unconventional concave-like pattern quantitatively describing a complex Pd(core)−Pt(shell) structure for the image seen in Figure 3c. Despite the clearly anisotropic growth of the binary cluster structure, in this case we were able to model it in good consistency with experiment as an icosahedral Pd core overcoated by a trilayer of Pt atoms (Figure 4b). This model, a gross simplification, demonstrates that even isotropic coverage of Pt on a Pd core reproduces the unusual intensity profiles observed with the HAADF-STEM simulations showing an inverted concave intensity profile (inset of Figure 4b) similar to what was found experimentally (inset of Figure 3d and Supporting Information Figure 9). It should be noted that a simulated monometallic Pd particle exhibiting the experimentally observed intensity profile can be produced. This latter case is easily discounted, however, because exclusion of the higher Z Pt scattering centers would require physically unreasonable nanoparticle geometries.

These results, then, lead us into an important conclusion pertaining to the templating effects of the various monometallic cores. With Pt at the core, we see essentially single-crystalline structures and tendencies toward uniform nucleated growth by the Pd atoms. In contrast, Pd cores promote irregular growth of the Pt shell, a result that amplifies the structural complexity of the nascent nucleating clusters. We also demonstrate the crystalline nature of the metal atoms in the shell regions rich in Pt (Figure 3c and Supporting Information, Figure 9)—a characteristic feature not seen for the monometallic Pd nanoparticles. This observation suggests that the Pt atoms might act to reconstruct the cluster motifs in these regions. Conversely, high Pd content regions appear to retain the high density of structural defects evidenced by the disordered cluster cores (Figure 1b and Supporting Information, Figures 5, 6, and 9). The data indicate that this tendency toward order is an element-specific property that is capable of strongly influencing secondary growth

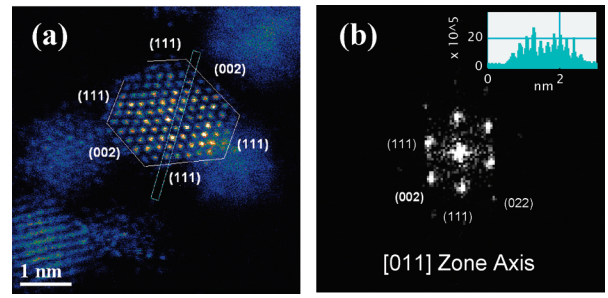

Figure 5. (a) Representative image of a coreduced bimetallic Pt−Pd nanoparticle with indexed facet planes (solid lines) and the areal intensity scanned region (boxed region). Power spectrum data for the coreduced sample with lattice planes and zone axes denoted with the integrated intensity measurement shown as the inset.

patterns, and may indicate the significance of subtle details of bonding in the differences seen in the catalytic behaviors of closely related alloy/binary compositions.[23,24,26,27]

A control experiment, conducted by the coreduction of Pt and Pd precursors, was performed to contrast the features seen in clusters formed through a random alloying of Pt and Pd atoms versus those of the organized core−shell structures described above. Panels a and b of Figure 5 show representative data for a Pt−Pd nanoparticle with Pt and Pd atoms statistically dispersed within the crystal and the derived diffraction pattern, respectively. The nanoparticle in this image is oriented along its [011] axis with randomly located regions of high and low contrast, indicating areas with a slight degree of phase segregation as well as adoption of an ordered, essentially single-crystalline, structure. The vast majority of the clusters in this sample were found to be oriented along their [011] zone axes with crystal facets defined by the (111) and (002) planes (Supporting Information, Figure 10). The high degree of crystallinity is striking given the general tendency toward defect incorporation evidenced by the monometallic Pd clusters. These coreduced samples resemble more the monometallic Pt and bimetallic Pt(core)−Pd(shell) clusters as they appear single crystalline complete with well-defined truncating edges. X-ray diffraction data collected for all the samples examined further iterates the degree of crystallinity embedded within these crystals (Supporting Information, Figure 11). Of note is the significant broadening of diffraction peaks for the monometallic Pd nanoparticles compared to all the other samples. In striking contrast, the diffraction data produced by the Pt−Pd alloy resulted in the sharpest Bragg peaks despite being the smallest of the bimetallic samples (~2.5 nm) indicating the dominance of Pt in the diffraction signals. The observed dispersion of the metal atoms seen here is expected given the miscibilities predicted by the Hume−Rothery rules: (1) the atomic radii are within 15% (1.4% for Pd and Pt, 1.37 and 1.39 Å, respectively); (2) both metals adopt an FCC packing structure; and (3), they have similar electronegativities (2.20 and 2.28 for Pd and Pt on the Pauling electronegativity scale, respectively).[39,54,55] Another interesting structural consequence revealed by these images is the placement of Pt and Pd atoms in direct juxtaposition, a structural feature unavailable in the idealized core−shell motifs. For example, an examination of the integrated intensities (the intensity profile inset of Figure 5b) show an oscillatory

(53) Vitos, L.; Ruban, A.; Skriver, H.; Kollar, J. *Surf. Sci.* **1998**, *411*, 186–202.
(54) Callister, W. *Materials Science and Engineering—An Introduction*, 7th ed.; Wiley: New York, 2006; p 84.
(55) Tao, F.; Grass, M.; Zhang, Y.; Butcher, D.; Renzas, J.; Liu, Z.; Chung, J.; Mun, B.; Salmeron, M.; Somorjai, G. *Sciencexpress* **2008**, 1.

pattern as modulated by the presence of both Pt and Pd atoms within the encased region of Figure 5a. Such qualitative features have recently been attributed to the formation of a random alloy in Pt−Co nanoparticles.[39] It is unquestionably clear, however, that the nanoalloys do not exhibit the structural features associated with a phase-segregated core−shell structure, a result validating the synthetic techniques implemented in this study and the deeply quenched metastable character of the energy landscape that serves to direct (and here preclude) the structural evolution of these materials.

Conclusions

To summarize, we have used C_s-corrected STEM imaging as a technique to distinguish between different nanoscale structural features in metal clusters. This has allowed the atomic characterization of structures in bimetallic Pt−Pd nanoparticles. Pt(core)−Pd(shell) clusters displayed strong intensity patterns concentrated at the center with weak scattering atoms along the periphery. Pd(core)−Pt(shell) nanoparticles show an inverted intensity map when compared to the Pt(core)−Pd(shell) sample, while the random nanoalloys studied reveal alternating intensities in their line scans. ZMULT simulations of the regular polyhedral structures commonly predicted for Pt and Pd nanoparticles verified that the dark-field detector dependence on heavy element scattering was the source of the experimentally observed variations in intensity. This emerging method of analysis offers the potential to provide important insights into the structures and compositional morphologies of nanoscale materials. We believe the methodologies described here will find broad application in studies of catalysis while advancing fundamental understandings of atomic bonding relevant to structure−function correlations.

Equally important, however, are the differences in crystallinity observed between the monometallic Pt and Pd nanoparticles. As was demonstrated, Pt atoms tend to activate the assembly of precise ordered features in a cluster, while Pd atoms were less effective in this respect. The observations developed here further provide future insights that will serve to guide the development of protocols that will yield more fully quantitative analyses of data of the type presented here, efforts that are in progress and that we hope to report shortly.

Acknowledgment. This work was sponsored in the part by the grants from the U.S. Department of Energy Grant No. DEFG02-03ER15476 (R.G.N.) and Grant No. DEFG02-01ER45923 (J.Z.). Experiments were carried out in part at the Frederick Seitz Materials Research Laboratory Central Facilities, University of Illinois, which is partially supported by the U.S. Department of Energy under Grants No. DE-FG02-07ER46453 and DE-FG02-07ER46471. The authors also thank Valeri Petkov for acquiring and interpreting the X-ray diffraction data in the Supporting Information.

Supporting Information Available: Supplementary images and tabulated data along with modeling schemes and diffraction data. This material is available free of charge via the Internet at http://pubs.acs.org.

JA9020952